Observed Global Mean State Changes Modulating the Collective Influence of the Tropical Atlantic and Indian Oceans on ENSO

VERÓNICA MARTÍN-GÓMEZ,[a] BELÉN RODRÍGUEZ-FONSECA,[b,c] IRENE POLO,[b] AND MARTA MARTÍN-REY[b,c]

[a] *Earth Science Department, Barcelona Supercomputing Center, Barcelona, Spain*
[b] *Earth Physics and Astrophysics Department, Universidad Complutense de Madrid, Madrid, Spain*
[c] *Instituto de Geociencias, CSIC, Madrid, Spain*

(Manuscript received 29 July 2023, in final form 25 March 2024, accepted 3 April 2024)

ABSTRACT: In the last decades, many efforts have been made to understand how different tropical oceanic basins are able to impact El Niño–Southern Oscillation (ENSO). However, the collective connectivity among the tropical oceans and their associated influence on ENSO are less understood. Using a complex network methodology, the degree of collective connectivity among the tropical oceans is analyzed focusing on the detection of periods when the tropical basins collectively interact and the Atlantic and Indian basins influence the equatorial Pacific sea surface temperatures (SSTs). The background state for the periods of strong collective connectivity is also investigated. Our results show a marked multidecadal variability in the tropical interbasin connection, with periods of stronger and weaker collective connectivity. These changes seem to be modulated by changes in the North Atlantic Ocean mean state a decade in advance. In particular, strong connectivity occurs in periods with colder than average tropical North Atlantic surface ocean. Associated with this cooling, an anomalous convergence of the vertical integral of total energy flux (VIEF) takes place over the tropical northwest Atlantic, associated with anomalous divergence of VIEF over the equatorial eastern Pacific. In turn, an anomalous zonal surface pressure gradient over the tropical Pacific weakens the trades over the western equatorial Pacific. Consequently, a shallower thermocline emerges over the western equatorial Pacific, which can enhance thermocline feedbacks, the triggering of ENSO events, and therefore, ENSO variability. By construction, our results put forward opposite conditions for periods of weak tropical basin connectivity. These results have important implications for seasonal to decadal predictions.

KEYWORDS: Atmosphere–ocean interaction; Large-scale motions; Climate variability; Multidecadal variability; Tropical variability

1. Introduction

El Niño–Southern Oscillation (ENSO) is the dominant interannual variability mode of the ocean–atmosphere coupled system, becoming the major source of predictability for the seasonal to interannual climate around the globe (McPhaden et al. 2006; Timmermann et al. 2018). It is widely accepted that ENSO has impact on the sea surface temperature (SST) anomalies of the adjacent tropical basins, such as tropical North Atlantic (TNA; Wu et al. 2020; García-Serrano et al. 2017; Wade et al. 2022) and Indian Ocean (Lau and Nath 2003; Wang and Wang 2014). In particular, ENSO phenomenon alters the Pacific–North American (PNA) pattern and tropical atmospheric circulation, weakening the trades over TNA and warming the sea surface via latent heat fluxes (Enfield and Mayer 1997; Klein et al. 1999; Giannini et al. 2001; García-Serrano et al. 2017; Wade et al. 2022). Several authors also argued that ENSO can induce a tropospheric warming inhibiting the convection over the tropical Atlantic and thus favoring ocean heat gain (Chiang and Sobel 2002; Chang et al. 2006). Regarding the Indian basin, the ENSO-induced anomalous Walker circulation produces descending motions over the eastern side, activating the Bjerknes feedback and contributing to the development of a positive Indian Ocean dipole (IOD; Wang and Wang 2014; Krishnamurthy and Kirtman 2003). However, ENSO's impact on the equatorial Atlantic has been found to be inconsistent due to the existence of counteracting effects (Latif and Grötzner 2000; Chang et al. 2006; Lübbecke and McPhaden 2012), ENSO asymmetries (L. Jiang et al. 2023), and favorable/unfavorable tropical Atlantic background state (Martín-Rey et al. 2018).

During the last decades, there is emerging evidence about the existence of remote precursors for ENSO phenomena. SST anomalies in TNA (Ham et al. 2013a,b), equatorial Atlantic (Rodríguez-Fonseca et al. 2009; Polo et al. 2015; Martín-Rey et al. 2014), and Indian Ocean (Saji et al. 1999; Izumo et al. 2010) could influence the equatorial Pacific SST variability. Each interbasin interaction occurs in a different season, in agreement with the seasonal cycle of the interannual variability of each particular basin. Thus, the equatorial Atlantic impact on ENSO occurs in boreal summer through an alteration of the

Supplemental information related to this paper is available at the Journals Online website: https://doi.org/10.1175/JCLI-D-23-0450.s1.

Corresponding author: Verónica Martín-Gómez, vero.martin.gomez@gmail.com

DOI: 10.1175/JCLI-D-23-0450.1

Walker circulation. The modified western equatorial Pacific easterly winds trigger the physical mechanisms associated with La Niña (El Niño) development for a warming (cooling) in the equatorial Atlantic (Rodríguez-Fonseca et al. 2009; Polo et al. 2015). Regarding the tropical North Atlantic impact on ENSO, it is maximum in boreal spring when a warming (cooling) of this region produces an equatorial atmospheric Rossby wave, due to the anomalous convection. It is translated into a surface anticyclonic response over the central Pacific, which produces anomalous currents advecting cold (warm) anomalies to the central Pacific, developing a La Niña (El Niño) (Ham et al. 2013a). Although there is some skepticism about the real existence of this teleconnection (Zhang et al. 2021), recent studies have provided further evidence about the important role of TNA persistence until boreal summer (Jiang et al. 2022) and the atmospheric Kelvin wave response over the Indian Ocean and Maritime Continent for enhancing the easterlies preceding ENSO phenomenon (Rong et al. 2010; Yu et al. 2016; S. Chen et al. 2022; Jiang and Li 2021; Ma et al. 2022). The impact of the Indian Ocean on ENSO takes place in boreal fall, when the IOD (Saji et al. 1999), an internal air–sea coupled mode of interannual variability, peaks. A positive IOD is characterized by cold anomalies in the eastern Indian Ocean and warm conditions over the western side, fostered by anomalous easterly winds in the central basin via the Bjerknes feedback (Webster et al. 1999; Saji et al. 1999). During boreal fall, a positive (negative) IOD alters the Walker circulation, generating anomalous westerly winds over the western Pacific, that contributes to El Niño (La Niña) development in the following winter season (Annamalai et al. 2010; Luo et al. 2010). Several authors have also reported an opposite-sign connection between ENSO and the occurrence of an IOD pattern 14 months in advance (Izumo et al. 2010, 2014). Thus, the existence of warming and cooling conditions in the tropical Atlantic and Indian basins, respectively, during previous seasons can promote the development of ENSO during the next winter.

Tropical basin interactions (TBIs) are, therefore, a new paradigm of research that highlights the need of an integrated view of the whole tropics to understand the climate variability from interannual to decadal time scales (Cai et al. 2019; Rodríguez-Fonseca et al. 2020). In this sense, and in contrast with previous studies that focused on individual basin precursors, the present study aims to provide a global picture of tropical ocean basins as a whole unique predictor of ENSO phenomena.

A remarkable feature of the TBIs is their nonstationary behavior, since they only occur in particular decades (Rodríguez-Fonseca et al. 2020; Martín-Rey et al. 2014, 2015; Polo et al. 2015; Wang et al. 2017; Cai et al. 2019; Ding et al. 2023; W. Chen et al. 2022; Park et al. 2023b). The causes of the decadal activation of the TBI are still under debate. Recent studies have refuted the idea of multidecadal behavior of tropical basins impacting ENSO (Jiang et al. 2021; F. Jiang et al. 2023). However, some studies have suggested the important role of changes in the oceanic and atmospheric background states, driven by the Atlantic multidecadal variability (AMV), the decadal variability of the North Atlantic Oscillation (NAO), or decadal variations in the ITCZ location (Martín-Rey et al. 2014; Ding et al. 2023; Losada et al. 2022) as a switch-on for TBIs. In addition, a modification in the spatial structure of the tropical interannual modes, together with an enhancement of equatorial variability and convection, has been suggested as a possible cause for the activation of TBI at multidecadal time scales (Martín-Rey et al. 2014, 2018; Wang et al. 2017; Losada and Rodríguez-Fonseca 2016; Cai et al. 2019; Losada et al. 2022; Ding et al. 2023).

The existence of TBIs opens windows of opportunity for improving the seasonal to decadal climate predictions. SST anomalies in the tropical Atlantic and Indian basins can enhance the predictability of ENSO through changes in the surface winds over the central and west tropical Pacific (Frauen and Dommenget 2012; Dayan et al. 2014; Losada and Rodríguez-Fonseca 2016; Exarchou et al. 2021). These anomalous surface winds can intensify the Bjerknes feedback giving rise to stronger ENSO events (Keenlyside et al. 2013; Wang and Wang 2021). Moreover, a statistical hindcast that includes the information about the air–sea coupled mechanism of the Atlantic–Pacific connection shows an increase in ENSO predictability during the first and last decades of the twentieth century (Martín-Rey et al. 2015). This multidecadal modulation of ENSO predictability can be understood by the nonstationarity feature of this interbasin linkage (Martín-Rey et al. 2014; Crespo-Miguel et al. 2023), which also coincides with decadal changes in ENSO properties and mechanisms (Grothe et al. 2020; Crespo et al. 2022; Weisheimer et al. 2022; Gan et al. 2023).

The aim of this study is twofold: (i) to analyze the TBIs as collective connectivity among the interannual variability modes that characterize the tropical oceans and which peaks before the ENSO peak (i.e., the Pacific is lagged up to 9 months with respect to the Atlantic and Indian Oceans) and (ii) to analyze the multidecadal variations of the connections identifying the global mean states associated with high connectivity.

In this study, the degree of collective connectivity among the tropical oceans is analyzed considering them as a nonstationary core, whose influence on ENSO can vary in time. In particular, we explore the variability of the degree of collective connectivity along the observational record, focusing on the detection of periods where the tropical oceans are more active interacting among them and influencing ENSO in the same calendar year. The favorable conditions that could lead to the nonstationary behavior of collective tropical basin interactions are also described. To do so, we consider a complex network perspective and construct a climate network in which each one of the nodes represents one of the main interannual variability modes that characterize the tropical oceans. In this way, the climate indices representative of these modes are Atlantic zonal mode (Atl3), Niño-3 (ENSO), IOD, and TNA. To investigate the TBIs and their variability, we calculate the mean network distance (Tsonis et al. 2007; Martín-Gómez and Barreiro 2015), a useful tool from complex network theory that provides a measure of the degree of collective connectivity among the tropical oceans, considering them as a core. Previous studies have analyzed the interaction between two tropical basins using moving window correlation analysis with a linear interdependence measure (Pearson's correlation coefficient; e.g., Rodríguez-Fonseca et al. 2009; Martín-Rey et al. 2014, 2015; Polo et al. 2015; Wang et al. 2017). Here, we make a step forward by utilizing a novel metric that allows for

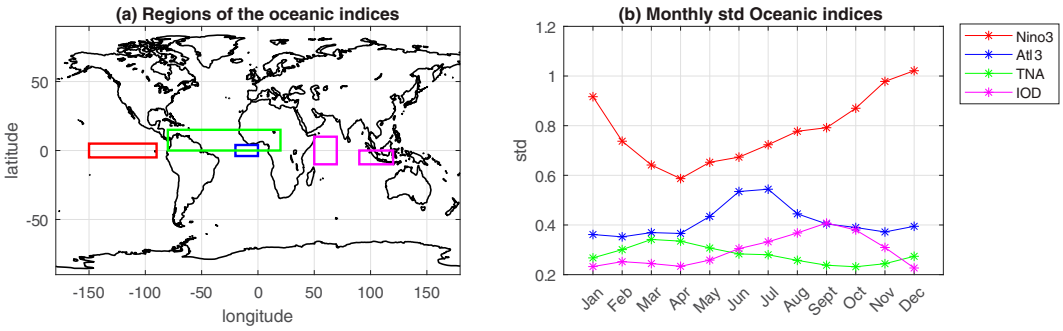

FIG. 1. (a) Domains of the network's nodes where the SST anomalies are averaged for computing the following indices: Niño-3 (red box), Atl3 (blue box), TNA (green box), and IOD (magenta boxes). For the case of the IOD, the index is constructed as the difference between the western and eastern boxes. (b) Monthly standard deviation of the Niño-3 index (red curve), Atl3 index (blue curve), IOD index (magenta curve), and TNA index (green curve). Values are computed from the monthly SST anomalies from HadISST during the period 1900–2010.

considering both the linear and nonlinear relationships underlying TBIs and enables the comprehensive analysis of all tropical basins collectively.

This study is organized as follows. The data and methodology considered in this study are introduced in section 2. In section 3, the results regarding (i) the collective connectivity among tropical oceans and its multidecadal variability, (ii) the favorable conditions that are related to periods of strong connectivity among tropical oceans, and (iii) the drivers leading periods of strong TBI are presented. Finally, section 4 comprises the main conclusions and the discussion of the results.

2. Data and methodology

a. Data

We consider monthly SST values from Hadley Centre Sea Ice Sea Surface Temperature database, version 1.1 (HadISSTv1.1; Rayner et al. 2003), with a spatial resolution of 1° × 1°, and also from NOAA Extended Reconstructed SST, version 5 (ERSST.v5; Huang et al. 2017), with a spatial resolution of 2° × 2°. Both datasets cover the period 1890–2019. In addition, we use monthly SST values from the ECMWF's first atmospheric reanalysis of the twentieth century (ERA-20C reanalysis; Poli et al. 2016) ranging from 1900 to 2010.

To analyze the changes in mean state and circulation that could lead or modulate the connectivity among the tropical oceans, we use the 3D velocity at different vertical levels of 1000, 900, 800, 700, 600, 500, 400, 300, 200, and 100 hPa; mean sea level pressure; zonal and meridional wind stress; and the zonal and meridional components of the vertical integral of the total energy flux (VIEF) from the ERA-20C reanalysis system during the period 1900–2010 (Poli et al. 2016). The zonal (meridional) component of VIEF represents the zonal flux of the total energy (sum of potential, kinetic, internal, and latent energies) integrated over the whole vertical column, that is, the vertical integral of the product between the zonal (meridional) wind and the total energy (Berrisford et al. 2011).

Moreover, we also consider the monthly values of the 20°C isotherm depth (z20) as a proxy of the thermocline depth over the period 1900–2008. We estimate the z20 from the Simple Ocean Data Assimilation (SODA) project, version 2.2.4 (Carton and Giese 2008). The SODA reanalysis uses the POP2.x ocean model. SODA data have 0.5° × 0.5° horizontal resolutions from 1871 to 2008 (we use the data for the period 1900–2008). A sequential assimilation algorithm is used with a 10-day updating cycle. NOAA Twentieth Century Reanalysis, version 2 (20CRv2), surface wind stress, and variables for the bulk formula are applied. It assimilates the World Ocean Database 2009 (WOD09) standard levels of temperature and salinity and SST from International Comprehensive Ocean–Atmosphere Data Set, version 2.5 (ICOADS 2.5).

b. Methodology

1) CONSTRUCTING THE CLIMATE NETWORK

To analyze the collective connectivity among the tropical oceans, we consider a complex network perspective and construct a climate network. For this purpose, we first need to define the nodes of the network (interactive agents) and the criterion through which we consider that two nodes are connected (interacting).

The climate network is constructed considering as nodes the main interannual variability modes that characterize the tropical oceans: TNA, Atl3, ENSO (Niño-3), and IOD. The specific domains for the nodes are (150°–90°W, 5°N–5°S) for Niño-3, (20°W–0°, 3°N–3°S) for Atl3, (80°W–20°E, 0°–15°N) for TNA, and (50°–70°E, 10°S–10°N) and (90°–110°E, 10°S–0°) for the western and eastern regions of the Indian Ocean, respectively, for the IOD (see longitude–latitude boxes in Fig. 1a).

Each one of these nodes is characterized by an index that represents the variability of the SST anomalies centered on the season of its peak of variability during the period 1900–2009: Niño-3 in November–January (NDJ), Atl3 in June–August (JJA), TNA in March–May (MAM), and the Indian Ocean dipole in August–October (ASO) (see Fig. 1b). SST anomalies are computed by removing the seasonal mean over the period 1900–2010. We then remove the linear trend of the anomalies considering the full period of study. In the case of the IOD, the index is constructed as the difference between the western box and the eastern box. For all cases, the indices are calculated for all SST databases, which cover the period 1900–2009

for ERSST.v5 and HadISSTv1.1 and the period 1910–99 for ERA-20C.

SST anomalies for each of the regions are spatially averaged in the corresponding peak season, and the linear trend is removed. After that, a Butterworth filter is applied to the indices using a cutoff frequency of 1/11 yr^{-1}. The obtained filtered anomalous SST indices (nodes) are then standardized. Finally, we consider that two nodes are connected when the Spearman correlation coefficient is statistically significant. The significance is established based on the Monte Carlo method, estimating the correlation thresholds that correspond to the 90% percentile for each pair of the network's nodes. For this purpose, 500 surrogate time series of each node are computed considering the nodes as red (white) noise if their autocorrelation at lag 1 year is (not) statistically significant in a one-tailed t test at the 95% confidence level.

The constructed network considers all nodes leading Niño-3: Atl3, IOD, and TNA, which are centered in JJA, ASO, and MAM seasons, respectively. Also, Niño-3 is considered for the following NDJ, which is the season of El Niño peak. Therefore, we could interpret the network as the group of nodes that interact together and influence ENSO.

2) Quantifying the degree of collective connectivity among tropical basins

Once the network is constructed, we focus on analyzing the degree of collective interaction among the network nodes. For this purpose, we use the mean network distance, a useful tool from the complex network theory that allows to quantify the degree of collective interaction among the network nodes and detects the period of maximum and minimum degree of collective connectivity (Tsonis et al. 2007; Martín-Gómez and Barreiro 2015). Mathematically, it is defined as

$$d(t) = \frac{2}{N(N-1)} \sum_{i<j} \sqrt{2(1 - |r_{i,j}|)}, \tag{1}$$

where N represents the number of network nodes (four in our case) and $r_{i,j}$ represents the correlation coefficient between the nodes i and j. Here, we use the Spearman rank correlation coefficient, which is computed considering a centered moving window with 21-yr length. The choice of 21 years was done by similarity with previous studies (Rodríguez-Fonseca et al. 2009; Martín-Rey et al. 2014, 2015; Polo et al. 2015). Nonetheless, the sensitivity of the results to the choice of the moving window length was tested considering moving windows from 15 to 29 years. It was found that the results are not sensitive to the moving window length chosen (not shown). The time step used for consecutive correlation is 1 year. Therefore, the mean network distance time series contains 89 values, each one of them representing the degree of collective connectivity considering a 21-yr moving window. For each moving window, Eq. (1) is itemized in six terms, each one of them representing the contribution to the mean network distance of each one of the six possible combinations among network nodes.

In Eq. (1), the absolute value of the correlation coefficient is utilized since this metric serves as a quantitative measure of the level of interaction between nodes, irrespective of the correlation's sign. The maximum (minimum) value of the mean network distance is $\sqrt{2}(0)$, which corresponds to a completely disconnected (connected) network. Therefore, the smaller the mean network distance, the larger the degree of collective connectivity among nodes. This measure has demonstrated its potential to detect periods of maximum/minimum connectivity among several nodes (Tsonis et al. 2007; Martín-Gómez and Barreiro 2015). Unlike most previous studies, in which authors analyze the interaction between two tropical basins using moving window correlation analysis with a linear interdependence measure (e.g., Rodríguez-Fonseca et al. 2009; Wang et al. 2017), our methodology allows us to work with all the tropical basins as a collective core and analyze its connectivity and variability.

Finally, synchronization periods are defined as temporal intervals during which the mean network distance falls below a predetermined threshold value. Consequently, we consider these periods to exhibit statistically significant collective interconnectivity among the tropical oceans. This threshold is computed by applying the Monte Carlo method to the nodes' indices. Surrogate time series of each node are computed, considering the nodes as red noise (white noise) if their autocorrelation at lag 1 year is (is not) statistically significant in a one-tailed t test at the 95% confidence level. Using these series, we compute 500 surrogate time series of the mean network distance, which allows determining the 5% level.

3) Background conditions associated with the tropical ocean basin connectivity

The mean network distance time series computed following section 2b can be understood as a low-frequency climate variability index. Focusing on it, we select three different periods in terms of the degree of collective tropical basin connectivity and analyze the favorable mean state background conditions associated with high (with respect to low) connectivity among the tropical oceans. Maps of mean differences in SST, mean sea level pressure (MSLP), Walker circulation, wind stress, and divergent components of the vertical integral of the total energy flux ($V_{\chi\text{–VIEF}}$) are used. The term $V_{\chi\text{–VIEF}}$ is used as a proxy of convection development in the atmosphere. Regions showing divergence (convergence) would be related to the development (inhibition) of convection (Green et al. 2019). In the case of the tropical areas, this would give an idea of the ITCZ position.

The term $V_{\chi\text{–VIEF}}$ is computed from the zonal and meridional values of the total energy fluxes integrated in all the vertical columns (VIEF), from ERA-20C reanalysis. To obtain the divergent components from the zonal and meridional components of VIEF, we first calculated the velocity potential χ_{VIEF} by solving Poisson's equation: $\nabla\mathbf{V} = \Delta\chi_{\text{VIEF}}$, where $\mathbf{V}$ is the vector with the zonal and meridional components of the VIEF and χ_{VIEF} is the associated velocity potential. Afterward, we computed the $V_{\chi\text{–VIEF}}$ gradient of χ_{VIEF} ($V_{\chi\text{–VIEF}} = \nabla\chi_{\text{VIEF}}$).

Monthly values of these variables are first annually averaged. Then, we compute the anomalies by subtracting the mean over the period 1900–2010 and remove the linear trend. Maps of mean differences were calculated as the difference between the mean of the anomalies of a specific field in a window belonging to the synchronized period minus the mean of the anomalies of the same specific field in a window belonging to the nonsynchronized

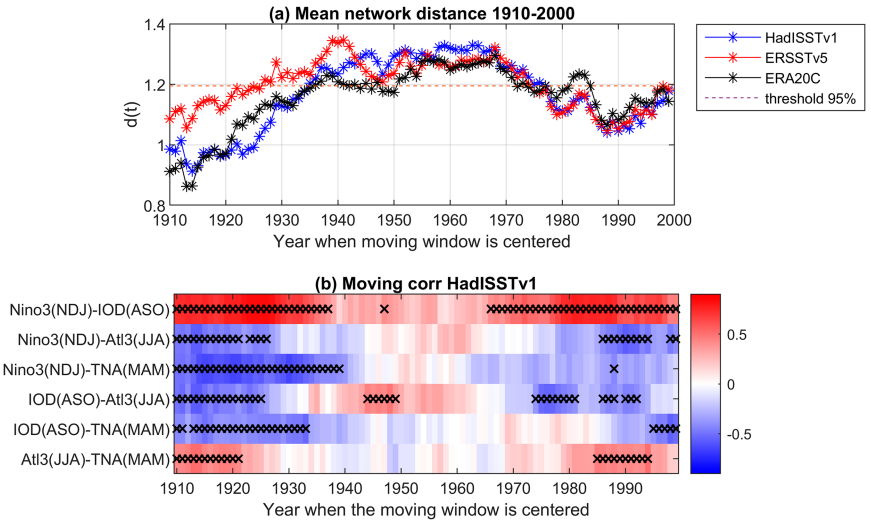

FIG. 2. (a) Mean network distance time series using SST from HadISSTv1 (blue line), ERSST.v5 (red line), and ERA-20C (black line). The red dashed line represents the threshold level considering a 95% confidence level in computing considering the Monte Carlo method. (b) Moving Spearman's correlation among each pair of nodes considering 21-yr moving windows. Windows are centered. Statistically significant values according to the Monte Carlo method are represented by black crosses. SST is from HadISSTv1.

period. We also compute annual average and linearly detrended z20 anomalies over the equator and compare the mean of the anomalies in two periods, one belonging to the synchronized period and the other belonging to the nonsynchronized period.

4) DETECTING DRIVERS FOR TBI DEVELOPMENT

To identify the drivers of the climate system that could lead to the development of periods of higher degree of collective tropical connectivity, we consider the mean network distance time series $d(t)$ as a low-frequency climate variability index and perform correlation maps between this index and the 21-yr running mean anomalies of global SST, MSLP, Walker circulation, wind stress, and the divergent components of VIEF. These correlation maps are computed with the atmospheric and oceanic fields leading the mean network distance from lag -9 to lag 0 (years). Correlation maps are multiplied by (-1), and therefore, they indicate the oceanic or atmospheric pattern that corresponds to an increase in connectivity (decrease in the mean network distance). By construction, the opposite maps will correspond to the spatial patterns promoting decrease in collective connectivity.

Statistical significance is evaluated considering an Ebisuzaki test (Ebisuzaki 1997), which is a nonparametric test used to estimate the statistical significance of correlation coefficients between time series with serial correlation. We consider a 90% confidence level.

3. Results

a. *Collective connectivity among the tropical oceans during the last century*

The degree of collective connectivity presents a large multidecadal variability, with two periods of strong connectivity during the last century: from 1910 to 1935 and from 1975 to 1998 (Fig. 2a). However, very low connectivity takes place in the decades in-between, from 1935 to 1975 (Fig. 2a).

To better understand the meaning of $d(t)$, correlation coefficients between each pair of network nodes are presented in Fig. 2b. The results depicted in Figs. 2a and 2b demonstrate that periods characterized by lower mean network distance values (Fig. 2a) align with increased significant connectivity among node pairs (Fig. 2b). Notably, Fig. 2b reveals that during synchronization periods, the Atl3, TNA, and IOD exert a significant influence on the SST anomalies in the equatorial Pacific (except TNA during the second synchronization period).

Furthermore, it is noteworthy that the majority of connections (Atl3–Niño-3, TNA–Niño-3, Atl3–IOD, and TNA–IOD) exhibit a transition from significant negative correlations (during synchronization periods) to nonsignificant correlations that even change in sign (during the disconnection period). Similar results are shown for Atl3–TNA, which shifts from positive correlation to nonsignificant positive/negative values. However, the IOD–Niño-3 connection exhibits positive correlation scores during synchronization periods and reduces its intensity becoming nonsignificant (but positive) during the nonsynchronization periods. There is an agreement between HadISSTv1.1 and ERSST.v5 datasets (Fig. 2a and Fig. S1 in the online supplemental material). Finally, the results in Figs. 2a and 2b are not sensitive to the choice of Niño-3, Niño-3.4, or Niño-4 index.

The nonstationary connectivity between tropical basins is shown in Figs. 2a and 2b. We now select three different periods: the synchronized periods P1 (1910–30) and P3 (1980–98) and the nonsynchronized period P2 (1950–70). These periods do not overlap among them and coincide with intervals of climate interest, as the climate shift reported in the tropical Pacific in 1976, which is in between P2 and P3 (Miller et al. 1994; Hare and Mantua 2000). Results do not differ when changing slightly

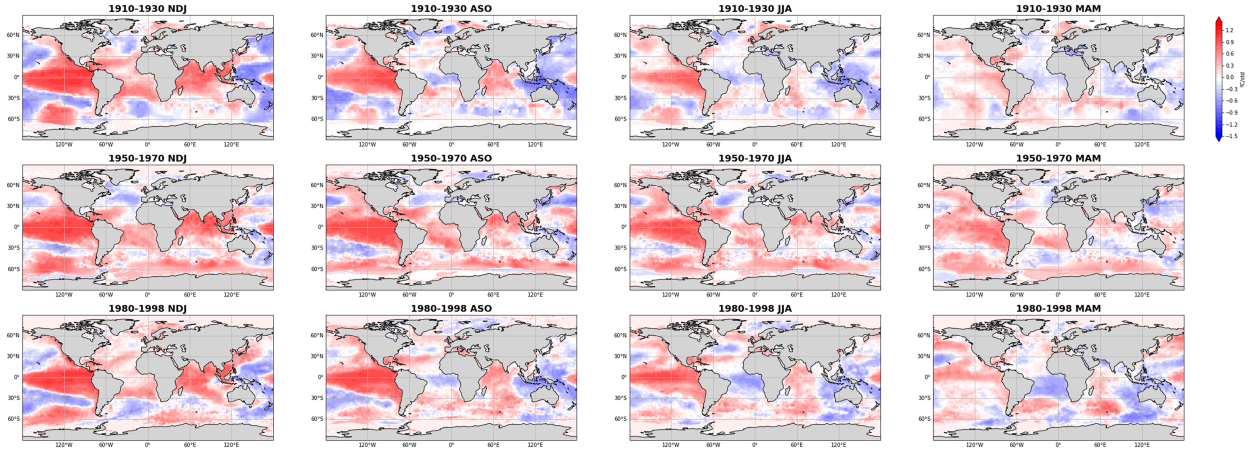

FIG. 3. Correlation maps of Niño-3 index in NDJ onto the SST anomalies during NDJ and the previous seasons (ASO, JJA, and MAM). (top) Period P1 (1910–30), (middle) period P2 (1950–50), and (bottom) period P3 (1980–98). Shaded areas are statistically significant considering the Monte Carlo test with a 90% confidence level.

the nonsynchronized period between the window centered in 1950 and 1960 in Fig. 2a. Period P2 corresponds to the window centered in 1960 in Fig. 2a, which represents a time interval of minimum tropical connectivity. Although years before the satellite era present uncertainties, especially prior to 1950s, they are also interesting to be analyzed because they have the advantage of avoiding the effects of global warming (Fig. 2a) and coincide with another climate shift in the 1920s–30s (Drinkwater 2006). Therefore, it is worth including them in the analysis, although due to the lack of observational data to be assimilated by the reanalysis, the results for this period should be analyzed with caution.

The nonstationary connectivity between tropical basins is also confirmed by the spatial correlation maps between Niño-3 NDJ and anomalous SST in NDJ and in the previous seasons (ASO, JJA, and MAM; see Fig. 3). Correlation maps are computed for the selected nonsynchronized period P2 and synchronized periods P1 and P3. During P2, an El Niño pattern in NDJ is associated with an anomalous warming in the Indian Ocean and western north and south tropical Atlantic, developed from MAM to NDJ (Fig. 3, left). Extratropical anomalies appear in the Southern Hemisphere in P2. On the contrary, in P1 and P3, tropical basin interactions prior to the development of ENSO are remarkable, with anomalous warm SSTs over the equatorial Pacific in NDJ significantly correlated with a positive IOD in ASO and negative SST anomalies in the equatorial Atlantic in JJA. Notice that an anomalous cooling over the TNA region in MAM is shown in P1 (Fig. 3), in contrast with P3, when there is no significant signal. This lack of negative and significant correlation in this 21-yr window is primarily understood by the dominant role of the equatorial Atlantic–ENSO linkage during the 1970s–90s and the delayed activation of the TNA–ENSO reported in the literature. The TNA–ENSO connection started becoming significant in the early 1990s (Rodríguez-Fonseca et al. 2009; Martín-Rey et al. 2014; Ham et al. 2013a; Wang et al. 2017; Park et al. 2023a,b). However, given that ERA-20C reanalysis only has available data from 1900 to 2010, we only can focus on the mean distance from 1910 to 1998. Remarkably, the ENSO-like SST anomalies are already present in boreal spring (MAM) and persist up to the winter season (NDJ) during P2 (Fig. 3, second row), which can suggest a persistent event from the previous winter season. However, in P1 and P3, anomalous equatorial Pacific SSTs started to develop in MAM, coinciding with an anomalous cooling in TNA and equatorial Atlantic, and are reinforced in the following seasons, boosted by the Atlantic zonal mode and IOD forcings (Fig. 3, second column). This result corroborates that other tropical basins (Atlantic and Indian) can favor the ENSO development in P1 and P3.

The above results provide evidence about the nonstationary behavior of the collective connectivity among tropical basins, existing periods when tropical basin interactions are strong (1910–35 and 1975–98) and the tropical Atlantic and Indian SSTs lead the ENSO peak, and periods when the tropical basins evolve independently and El Niño presents stronger persistence with no interactions of other tropical basins in the seasons before the peak (1935–75). In the following section, we investigate the global background conditions associated with periods of high connectivity.

b. Background conditions favoring the tropical ocean basin connectivity

1) COMPARISON OF 1980–98 (P3) VERSUS 1950–70 (P2)

Overall, the climatological conditions of P3 are characterized by colder extratropics and warmer tropics than in P2 (Fig. 4a). In particular, a negative Atlantic multidecadal oscillation (AMO)-like SST pattern emerges over the Atlantic Ocean for periods of strong connectivity (the opposite for weak connectivity; Fig. 4a). The cooler TNA region coexists with the warmer equatorial Indian and Pacific basins. Notice that an east–west SST gradient appears over the central Pacific with warmer anomalies over the eastern part.

Regarding sea level pressure, a positive NAO-like configuration is shown over the North Atlantic in agreement with an intensification of northeasterlies and an underneath sea surface cooling (Li et al. 2013; Martín-Rey et al. 2018) during the

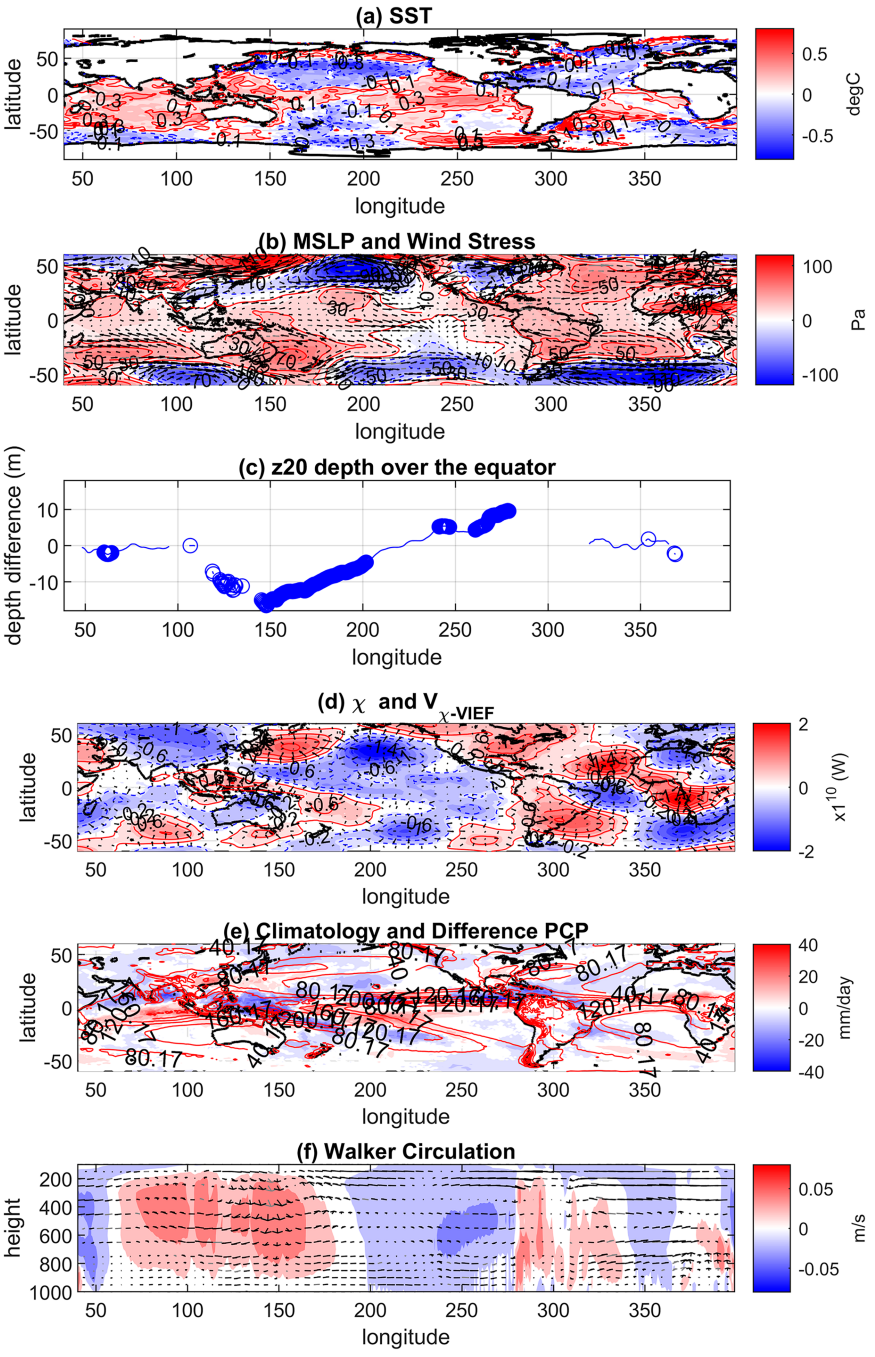

FIG. 4. Mean difference maps computed as the difference between the mean values in P3 and the mean values over P2 of (a) SST (contours), (b) MSLP (contours) and wind stress (arrows), and (c) thermocline depth (m) for the z20 averaged over 5°N–5°S. Negative (positive) values mean shallower (deeper) thermocline. (d) VIEF (contours) and $V_{\chi\text{–VIEF}}$ (arrows), (e) precipitation (shaded), and (f) Walker circulation (arrows). Shaded areas in (e) and (f) represent climatology. Shaded regions in (a), (b), and (d), circles in (c), and black arrows in (b) and (f) are statistically significant considering a 90% confidence interval.

period of tropical connectivity (Figs. 4a,b). Although the tropics present a general increase in SLP, a relative minimum appears over the central equatorial Pacific, producing two anomalous zonal pressure gradients: one that strengthens the easterlies in the easternmost side of the basin (230°–270°E) and another one that weakens them in the western–central equatorial Pacific (150°–230°E) (Fig. 4b). In addition, a shallowing of the thermocline takes place over this region, which is consistent with the divergence of winds produced by these SLP gradients. The weakening (strengthening) of the easterlies in the western (eastern) equatorial Pacific during the period of connectivity is consistent with the development of a shallower (deeper) thermocline over this region (Fig. 4c). Some authors have discussed how, under this background state, characterized by a shallower thermocline, the Bjerknes feedback is more efficient (Trascasa-Castro et al. 2021; Crespo et al. 2022).

Figure 4d shows χ_{VIEF} and its associated $V_{\chi\text{–VIEF}}$. Regions of anomalous $V_{\chi\text{–VIEF}}$ divergence are usually related to the location of anomalous wetter conditions as a region of anomalous energy transport divergence (Green et al. 2019) being a diagnostic used to locate the ITCZ. The opposite occurs for regions of convergence. In our results, and during the period of tropical connectivity, two anomalous centers of convergence $V_{\chi\text{–VIEF}}$ appear over the tropical Atlantic (over the northeast American coast and over Senegal–Mauritania Coast; Fig. 4d), which coincide with regions of anomalous sea surface cooling (cf. Figs. 4a,d). This anomalous convergence of $V_{\chi\text{–VIEF}}$ over the tropical North Atlantic occurs together with a northwest–southeast $V_{\chi\text{–VIEF}}$ anomalous divergence band that extends from the western equatorial Pacific (around 170°E) to the southeast tropical Pacific (around 20°S, 250°E) (Fig. 4d). Over the tropics, those regions where anomalous divergence of $V_{\chi\text{–VIEF}}$ develops (Fig. 4d) coincide with regions with an anomalous increase in the precipitation (Fig. 4e) and vice versa. The location of these divergence centers together with that of the regions of positive region suggests that during periods of more tropical basin connectivity, there is an equatorward displacement of the ITCZ over the western equatorial Atlantic (between 320° and 350°E) and Pacific (between 160° and 200°E, and around 240°E) and an eastward displacement of the South Pacific convergence zone (SPCZ), which is the northwest–southeast precipitation band that extends from the western equatorial Pacific (around 0°, 170°E,) to the southeast tropical Pacific (around 20°S, 250°E) (Figs. 4d,e).

Moreover, this period of strong connectivity is characterized by a weakening of the Pacific Walker circulation, as shown in Fig. 4f. Over the Maritime Continent, the strong climatological upward branch is debilitated and is associated with anomalous subsidence around 140°E (Fig. 4f). This downward motion agrees with a reduction in rainfall and the spatial distribution of precipitation and χ_{VIEF} anomalies (Figs. 4e,d). Over the equatorial Pacific, anomalous upward (downward) motions are found over 170°E–250°W (250°–320°E), which are consistent with the equatorial anomalous divergence (convergence) of the $V_{\chi\text{–VIEF}}$ (cf. Figs. 4d,f), the distribution of anomalous precipitation anomalies on the equator (Fig. 4e), and the anomalous MSLP pattern (Fig. 4b). The latest suggests anomalous convergence of winds over the equatorial Pacific around 230°E (Fig. 4f), which is in agreement with the convergence of zonal winds at lower levels in the Walker circulation (Fig. 4f). Moreover, the anomalous wind stress divergence observed over 150°E (Fig. 4b) is also consistent with the anomalous upward motions over there in the Walker circulation (Fig. 4f).

Therefore, the oceanic and atmospheric background conditions that promote collective tropical connectivity of the tropical basins are (i) a cooler north tropical Atlantic (Fig. 4a) that co-occurs with an anomalous convergence of the $V_{\chi\text{–VIEF}}$ over the western North Atlantic (around 40°–50°N, over the northeastern American coast) and warmer tropics with a divergence of the $V_{\chi\text{–VIEF}}$ over the equatorial regions; (ii) an equatorward displacement of the western Pacific and Atlantic ITCZ (Fig. 4e) and an eastward displacement of the SPCZ (Figs. 4d,e). Both displacements provide anomalous wetter conditions over most of the equatorial western Pacific. (iii) A center of relative lower pressure anomalies over the equatorial Pacific (around 250°E) produces two zonal MSLP gradients over the equatorial Pacific, which weakens (strengthens) the trade winds over the western (eastern) equatorial Pacific (Fig. 4f), reducing the pilling of water over the warm pool and causing the thermocline to rise (deepen) over the western (eastern) equatorial Pacific (Fig. 4c). The combination of an equatorward ITCZ and a shallower thermocline (which favors the ENSO development) could promote favorable conditions for other tropical basins to influence ENSO variability and, therefore, to develop a stronger collective connectivity among the tropical basins. By construction, the opposite takes place in periods of noncollective tropical basin interactions.

2) Comparison of 1910–30 (P1) versus 1950–70 (P2)

A similar behavior takes place in the synchronized period P1, during the beginning of the twentieth century, compared to P2. A cooling around the regions of the northern subtropical gyres takes place in agreement with an increase in SLP over these atmospheric anticyclonic circulations (Figs. 5a,b), as in P3 (Figs. 4a,b). Ekman transport produces a relative warming in the center of these gyres. A concomitant equatorial Pacific a warming emerges in agreement with a relative decrease in SLP in the center of the basin, in consonance with an enhancement of the surface wind convergence (Fig. 5b). This configuration could be due to the impact of the North Atlantic on the equatorial Pacific by alteration of the Hadley circulation. As a consequence of the equatorial wind convergence and the SLP gradient over the central Pacific, the trades weaken in the western part where the thermocline becomes shallower, while it deepens over the eastern equatorial Pacific (Fig. 5c).

Our results have identified the atmospheric and oceanic mean states that characterized those periods with more collective connectivity. However, the origin of these background conditions is still unclear. Several authors have suggested the AMV as a possible modulator considering just a single node of the TBI. In this way, Martín-Rey et al. (2014) identified how the equatorial Atlantic and Pacific could interact together for negative phases of the AMV, while Wang et al. (2017) analyzed how

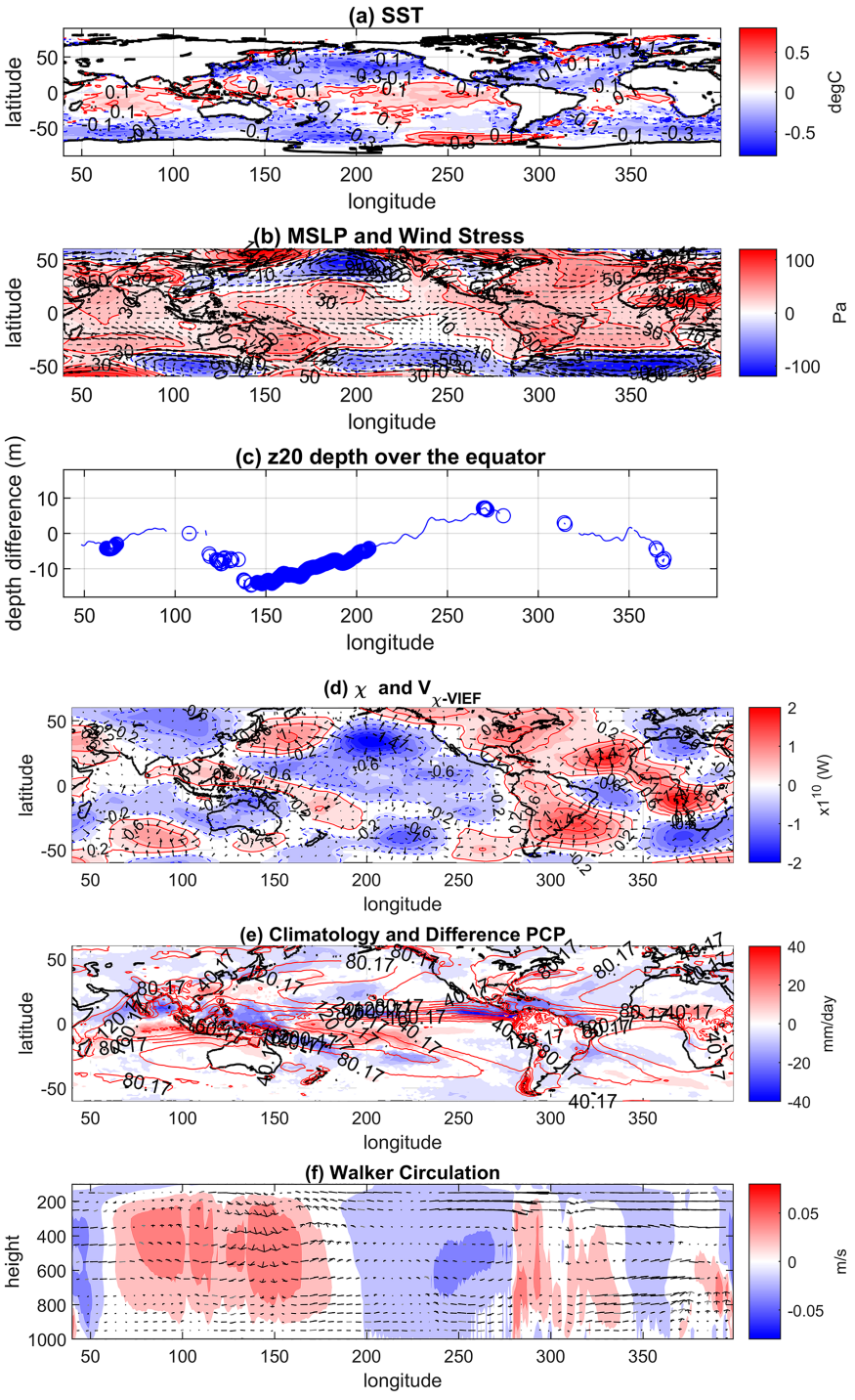

FIG. 5. Mean difference maps computed as the difference between the mean values in P1 and the mean values over P2 of (a) SST (contours), (b) MSLP (contours) and wind stress (arrows), and (c) thermocline depth (m) for the z20 averaged over 5°N–5°S. Negative (positive) values mean shallower (deeper) thermocline. (d) VIEF (contours) and $V_{\chi\text{–VIEF}}$ (arrows), (e) precipitation (shaded), and (f) Walker circulation (arrows). Shaded areas in (e) and (f) represent climatology. Shaded regions in (a), (b), and (d), circles in (c), and black arrows in (b) and (f) are statistically significant considering a 90% confidence interval.

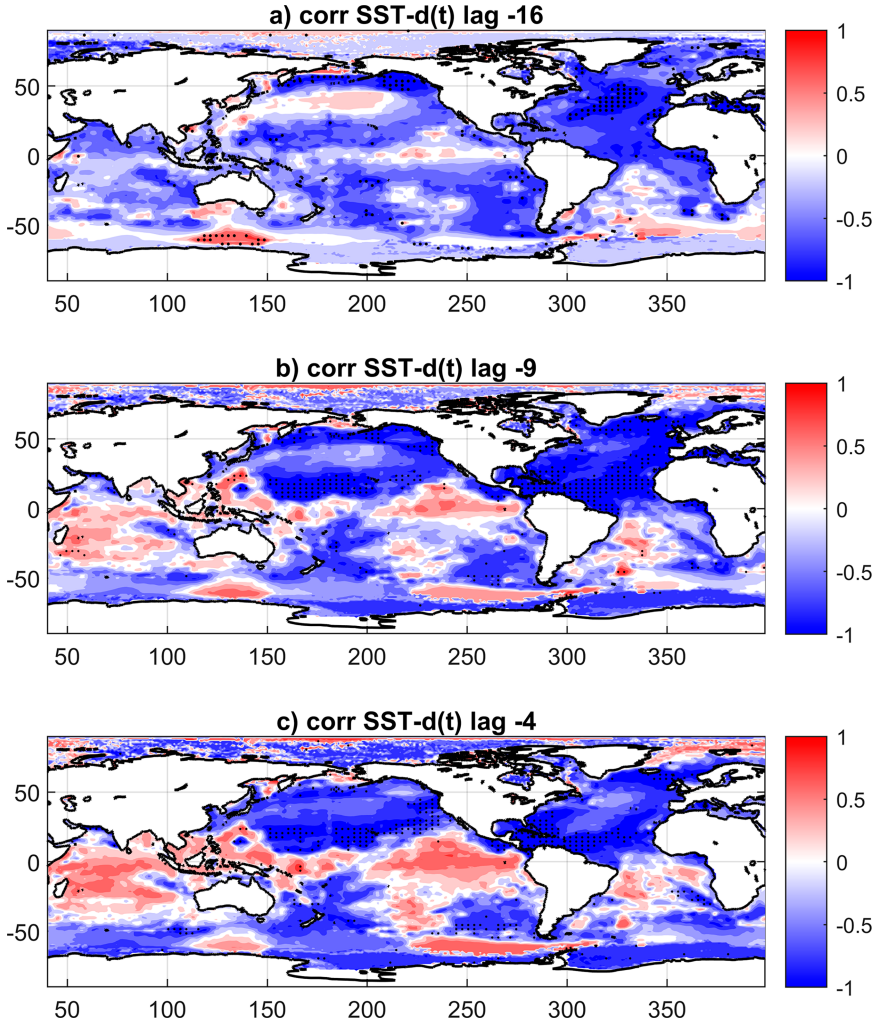

Fig. 6. Correlation maps of the degree of collective connectivity onto anomalous (a) SST at lag −16, (b) SST at lag −9, (c) SST at lag −4, (d) VIEF and V-VIEF at lag −9, (e) VIEF and V-VIEF at lag −4, (f) MSLP and wind stress at lag −4, and (g) MSLP and wind stress at lag 0. Dots in (a)–(c), black arrows in (f) and (g), and shaded areas in (d)–(g) represent correlation values that are statistically significant considering an Ebisuzaki test with a 90% confidence level. Lag −9 (−4) means that the atmospheric or oceanic field is leading 9 (4) years in the degree of collective connectivity. Positive (negative) correlation values suggest that an increase in the collective connectivity among the tropical oceans is related to an increase (decrease) in the atmospheric field.

during the positive AMV phase the tropical North Atlantic impact on ENSO was enhanced. Nevertheless, the emergent global ocean picture discussed in the present work presents several SST anomalies interacting with ENSO that merit consideration (Fig. 4a). Recent findings, based on model sensitivity experiments, have put forward how the equatorward displacement of the ITCZ can produce a flattening of the thermocline depth promoting tropical Atlantic impact on ENSO (Losada et al. 2022). Nevertheless, no work has focused so far in the collective connectivity among tropical basins and their associated influence on ENSO neither in the origin of the background conditions promoting them. In the next section, we dig into the physical processes leading to favorable conditions for collective connection among the tropical oceans using observations.

c. *Evolution of background conditions preceding collective tropical interbasin interactions*

To understand the origin of the background conditions described in the previous sections and detect possible drivers leading to the subsequent development of high tropical connectivity, as well as to investigate the physical mechanism for TBIs, we perform a correlation analysis between the degree of collective connectivity and the different oceanic/atmospheric fields from previous years leading to the activation of TBI. Correlation maps show a statistically significant cooling over the North Atlantic region that starts at lag −16 (years) and extends toward the tropical latitudes from lag −13, persisting until lag −4 (see Figs. 6a–c as examples; see Fig. S2). The SST structure resembles a negative AMO-like pattern

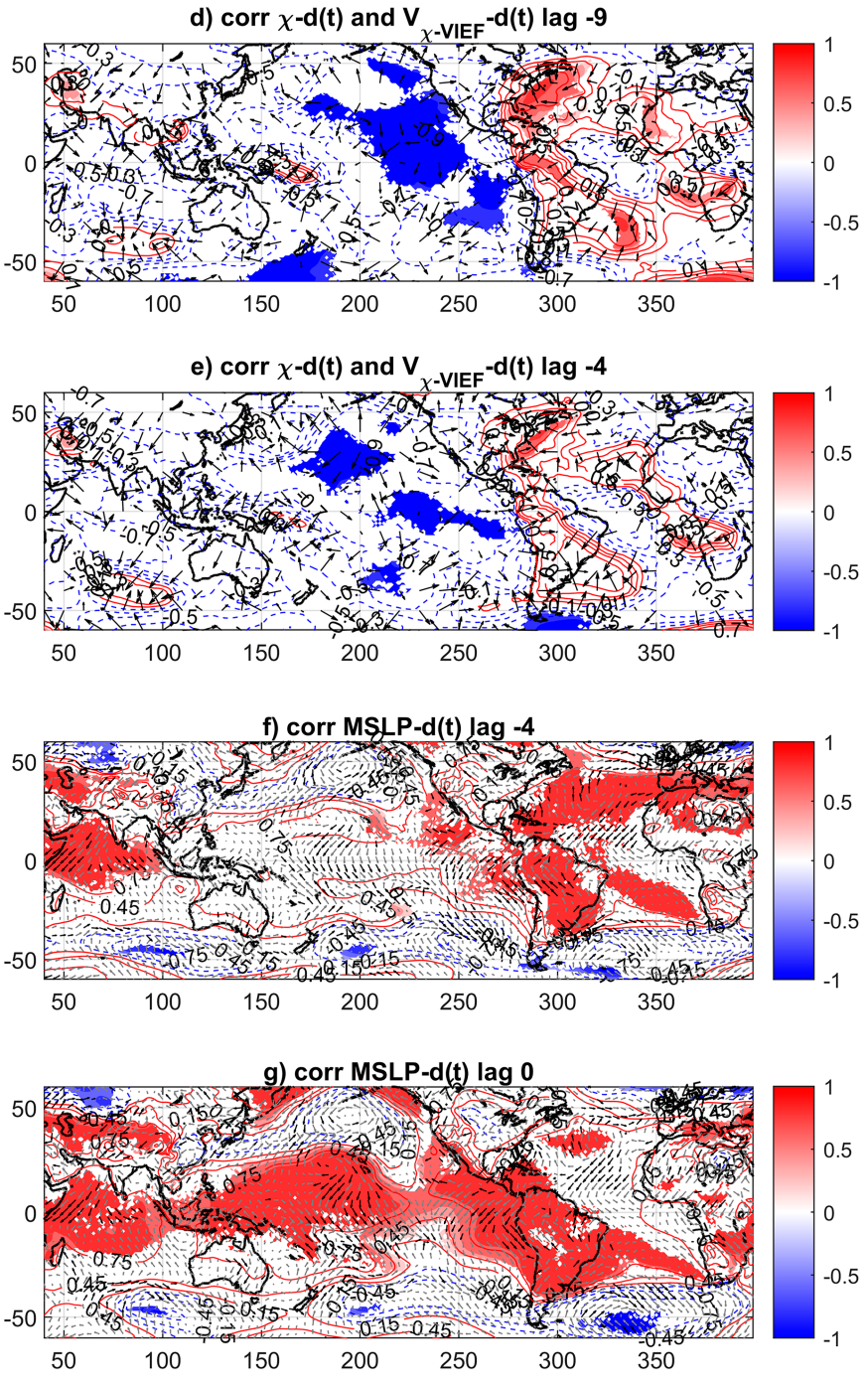

FIG. 6. (Continued).

that could act as the decadal precursor for favorable future conditions for tropical connections.

A possible mechanism linking the subtropical North Atlantic cooling with the subsequent development of warmer anomalies over the equatorial Pacific (Figs. 6a–c) could be through anomalous changes in the zonal and meridional overturning atmospheric circulations and in the ITCZ location. The persistence of the cooler SSTs over the subtropical North Atlantic from 13 up to 4 years before appears associated with the development of a statistically significant anomalous convergence of $V_{\chi\text{–VIEF}}$ over the northeast American coast and western Senegal–Mauritania Coast (see Figs. 6a–e). These anomalies over the North Atlantic appear together with a strong anomalous $V_{\chi\text{–VIEF}}$ divergence over the central–eastern

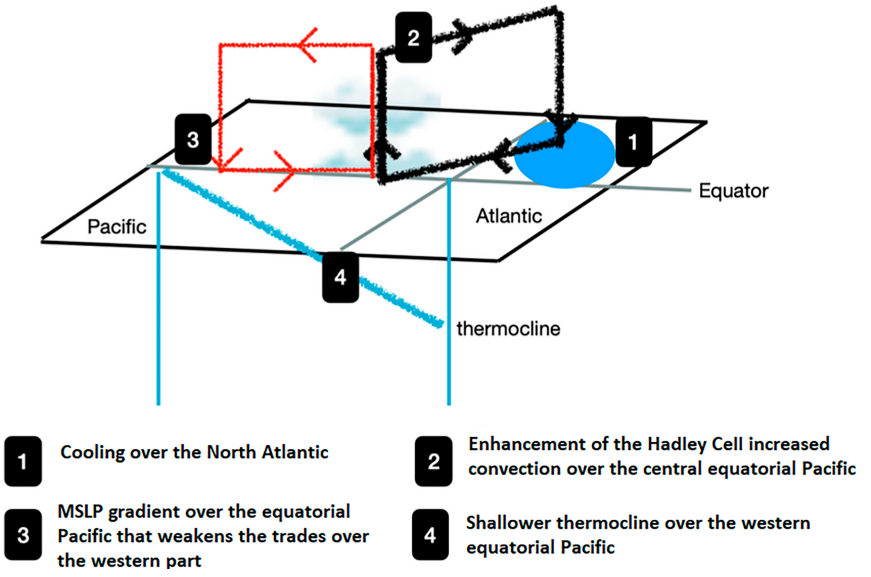

FIG. 7. Schematic for the origin of background conditions promoting collective TB connectivity and enhancement of ENSO variability: condition 1 takes place 16 years ahead, condition 2 from 9 to 4 years ahead, and conditions 3 and 4 from 4 to the years in which the connectivity among tropical basins is maximum.

tropical Pacific (Figs. 6d,e) around 200–270°E, which persists until lag −4.

The persistence of this anomalous $V_{\chi\text{–VIEF}}$ divergence over the equatorial Pacific (Figs. 6d,e) would be associated with the appearance of significant MSLP anomalies afterward over the equatorial Pacific (Figs. 6f,g). The anomalous MSLP pattern displays two gradients: one that weakens the trades over the western equatorial Pacific and another that strengthens them over the eastern part (Figs. 6f,g, also in agreement with Figs. 4b and 5b). This, in turn, could induce a shallower thermocline depth over the western equatorial Pacific (Fig. 4) and enhance thermocline feedbacks, triggering ENSO events (Trascasa-Castro et al. 2021). These conditions are favorable for the development of periods of strong connectivity. Figure 7 shows a scheme illustrating the mechanism aforementioned.

The present results put forward a possible role of the AMV, from 16 years in advance, on the equatorial Pacific background conditions, the latter being responsible for changing the ocean and atmospheric conditions for ENSO development, in a way that the other equatorial modes of variability can interact with it.

The role of AMV has been already proposed as a low-frequency precursor for TNA–ENSO and Atl3–ENSO interactions (Martín-Rey et al. 2014; Wang et al. 2017). However, our results highlight the need for a global ocean footprint to trigger collective tropical connectivity. Indeed, Fig. 8a shows evidence that the SST patterns shown in Fig. 6 represent the multidecadal variability of the Atlantic and Pacific Oceans. Positive IPO (depicted in Fig. 8b) is negatively and simultaneously related to grid distance (red line in Fig. 8a), while positive AMV (depicted in Fig. 8c) is positively related to grid distance from 16 years earlier (blue line in Fig. 8a), lending strength to its crucial role as a precursor to TBI. The results addressed here only allow us to hypothesize the physical mechanisms that might lead to the degree of connectivity among tropical oceans. A further study would be needed using model experiments in order to fully prove the linkage suggested in this study.

4. Conclusions and discussion

A complex network perspective has been used in this study to analyze, for the first time, the collective connectivity among the tropical oceans, focusing on the Atlantic and Indian Ocean leadership on ENSO during the calendar year and its variability during the last century.

This new methodology reveals that the collective connectivity among the tropical oceans exhibits a large multidecadal variability, bringing to light the existence of two periods of strong collective connectivity, at the beginning (1910–30) and end of the twentieth century (1980–98), and a period of disconnection in the decades in-between (1950–70). During periods of strong connectivity, the tropical Atlantic and Indian Oceans (characterized by the Atl3, TNA, and IOD modes and respective indices) are significantly correlated with Niño-3, suggesting that during these periods an external forcing could increase the equatorial Pacific variability.

We have also characterized the background conditions favorable for the development of collective tropical interbasin connectivity (Figs. 4–6 and 8). A cooler north tropical Atlantic co-occurs with an anomalous convergence of the $V_{\chi\text{–VIEF}}$ over the western North Atlantic (around 40°–50°N, over the northeastern American coast) and equatorward displacement of the western Pacific and Atlantic ITCZ and an eastward displacement of the SPCZ.

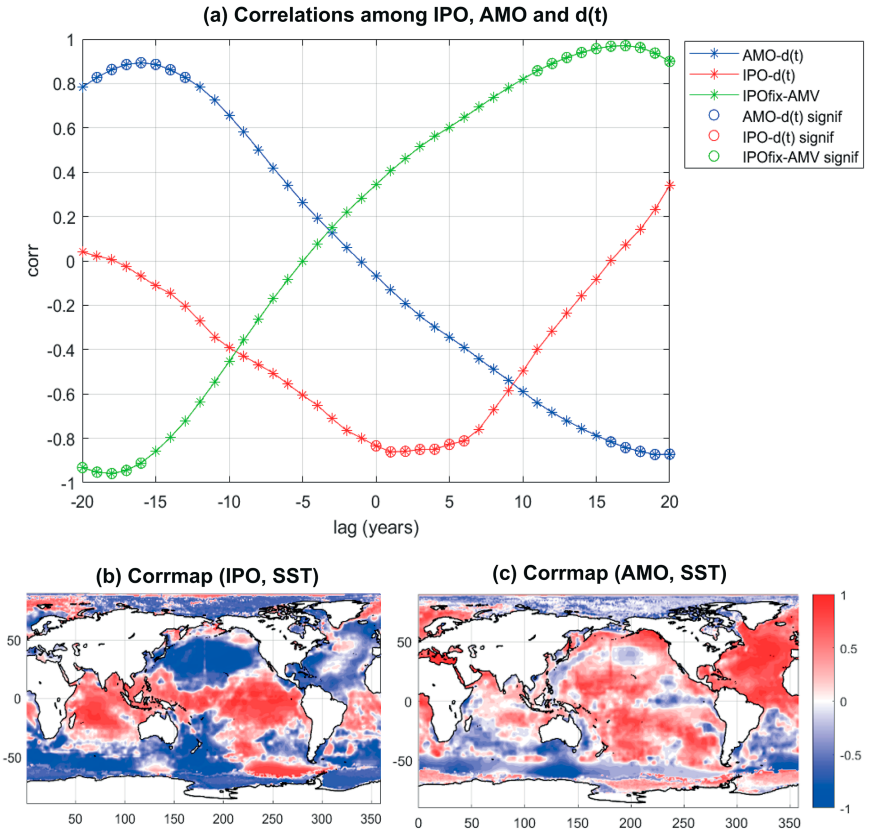

FIG. 8. (a) Correlation between AMO and network distance $d(t)$ (blue line) and between IPO and network distance (red line). Negative lags mean AMO or IPO leading network distance. Correlation between AMO and IPO (green line); in this case, negative lags mean AMO leading IPO. Circles represent correlation values that are statistically significant considering a 90% confidence level using an Ebisuzaki test. (b) Correlation between IPO index and SST. Positive IPO is related to warmer anomalies over the equatorial Pacific and cooler anomalies over the northwestern and southwestern Pacific. (c) Correlation between AMO index and SST. Positive AMO is related to anomalous warming over the North Atlantic region.

Both displacements provide anomalous wetter conditions over most of the equatorial western Pacific. Additionally, the zonal MSLP gradients developed over the equatorial Pacific weaken (strengthen) the trade winds over the western (eastern) equatorial Pacific, causing the thermocline to anomalously rise (deepen) over the western (eastern) equatorial Pacific. Shallower thermocline could induce more thermocline feedbacks and therefore higher ENSO variability during periods of higher collective connectivity.

We have also investigated the preceding conditions that lead to collective tropical interbasin interactions. Through a correlation map analysis, we find that the development and persistence of the cold anomalies in the tropical North Atlantic are associated with the development of (i) anomalous $V_{\chi\text{–VIEF}}$ convergence over the tropical northwest Atlantic and (ii) an anomalous $V_{\chi\text{–VIEF}}$ divergence over the tropical eastern Pacific. The persistence of the SST signal over the tropical North Atlantic would be making the divergence of the $V_{\chi\text{–VIEF}}$ over the eastern Pacific to persist also in time. Moreover, it would be also related to gradual increase in the MSLP over the region as the lag time reduces. The anomalous increase in MSLP spread along the tropical Pacific from lag −4, developing an anomalous zonal pressure gradient that weakens the trades over the western equatorial Pacific and strengthens them over the eastern part. This, in turn, would induce a mean state associated with connectivity (Figs. 4 and 8).

Although P1 and P3 periods illustrate a similar mean state compared to P2 (Figs. 4 and 5), the processes of their interannual variability may be different. This is discussed below.

We first look at the zonal wind stress variability changes in every period with respect to P2 (Fig. 9a). The zonal wind stress variability over the eastern (235°–265°E) and western (130°E–180°) equatorial Pacific regions is enhanced during the most connected periods P1 and P3 (Fig. 9a). Remarkably, the zonal winds in these key regions are influenced by the other tropical basins. During P1 and P3, Atlantic SST indices (TNA and Atl3, fixed in MAM and JJA, respectively) are able to impact the Pacific winds in both the eastern and western regions during the following seasons (solid and dashed green and blue lines in Figs. 9b,c). This interbasin

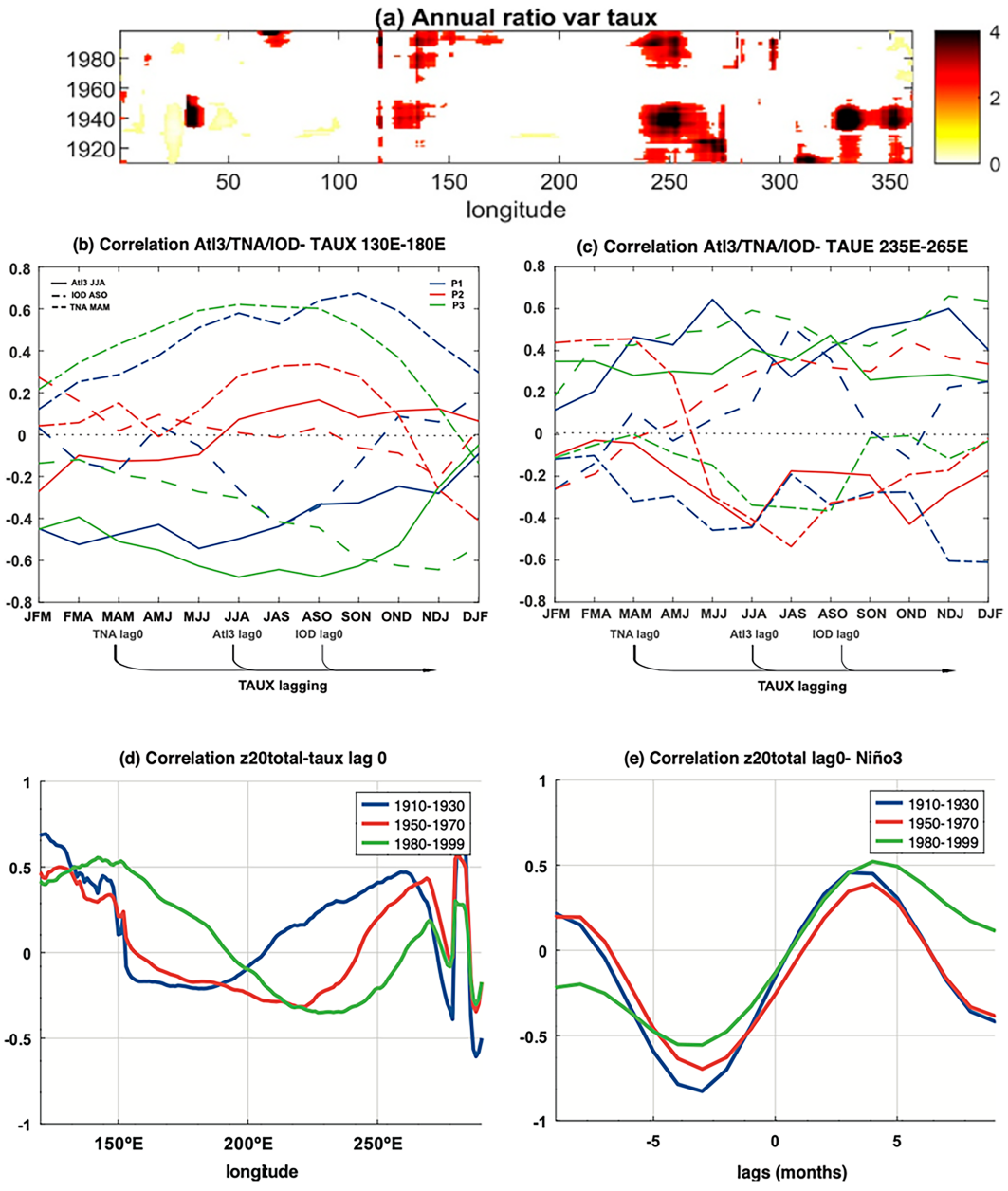

FIG. 9. (a) Ratio of the variance of the zonal wind stress at the equator for all periods (centered) and the total variance. (b) Lead–lag correlation in the advanced 21-yr window between SST anomalies in TNA in MAM (dashed line), Atl3 in JJA (solid line), and IOD in ASO (dashed–dotted line) and seasonal zonal wind stress anomalies in the equatorial western Pacific (130°E–180°) from January–March (JFM) to DJF. Positive lags are those seasons following the peak of each SST index, indicating that zonal wind is lagging. (c) As in (b), but for equatorial eastern Pacific (235°–265°E) zonal wind stress anomalies. (d) Correlation between z20 averaged over the equatorial Pacific (5°N–5°S; 130°E–90°W) and the zonal wind along the equatorial Pacific (5°N–5°S) for the three periods commented along the text. P1 and P3 are periods of interbasin connection, and they are represented in blue and green lines, respectively. (e) Correlation between z20 averaged over the equatorial Pacific (5°N–5°S; 130°E–90°W) at lag 0 and Niño-3 index lagging (positive lags) and leading (negative lags) for the three periods.

contribution is strengthened by a decadal situation in the Atlantic according to a previous study by Martín-Rey et al. (2014). Additionally, the Indian index also influences the zonal wind in the western and eastern Pacific during both, P1 and P3, synchronized periods (dashed–dotted blue and green lines in Figs. 9b,c).

These zonal winds on interannual scales affect the ENSO evolution through the alteration of equatorial thermocline.

The zonal wind stress relates to the equatorial Pacific thermocline in different ways: In P1, it is the wind over the eastern region that impacts z20 (positive correlations in blue line in Fig. 9d), while in P3 it is the wind over the western region that impacts z20 (positive correlations in green line in Fig. 9d). However, the linkage of z20 wind is drastically reduced and even reversed in P2 (Fig. 9d, red line). Although for all three periods the increase in z20 will lead to the positive SST of the Niño-3 region (Fig. 9e), only during P1 and P3 the interbasin connections are established (Fig. 2). This can be understood by the favorable mean state and enhanced zonal wind variability during those decades, which could favor the stronger coupling with the ocean dynamics (z20) underlying ENSO development as explained.

In addition to this evidence on the connection between zonal wind stress over the equatorial Pacific and SST indices, especially in the P3 period, the mean zonal MSLP gradients developed over the equatorial Pacific weaken (strengthen) the trade winds over the western (eastern) equatorial Pacific, causing the mean thermocline to anomalously rise (deepen) over the western (eastern) equatorial Pacific. If the mean thermocline is shallower in the western equatorial Pacific, it is easier for a wind forcing to develop ENSO events through the thermocline feedback (Trascasa-Castro et al. 2021). Both factors, shallower mean thermocline (Fig. 4c) and increased wind stress variability (Fig. 9a), may cooperate to enhance SST variability over the equatorial Pacific and therefore ENSO variability in P3. This increase in wind stress could be caused by Atl3, TNA, and IOD; however, no clear evidence was found regarding the possible influence of the changes in the variance in Atl3, TNA, and IOD in the enhanced correlation between these basins and the zonal winds over the tropical Pacific (Figs. 9b,c). A further study would be needed to elucidate this question.

Regarding changes in the ENSO characteristics during the twentieth century, there are several works that have reported observed changes that agree with our results, as the variance increased from the 1980s (An and Wang 2000; Gan et al. 2023; Crespo et al. 2022; Weisheimer et al. 2022) and also modeled with simple stochastic linear models (Crespo et al. 2022). In particular, Crespo et al. (2022) and Crespo-Miguel et al. (2023) have demonstrated that ENSO can be represented as a full recharge oscillator during the period coinciding with our last (P3) synchronization period (1980–98). This can be understood by a stronger impact of warm water volume (WWV) on SSTs, which suggests that during this period, WWV is a good predictor for ENSO events.

It is shown here that there is a coherent mean state associated with more collective connectivity (Figs. 4 and 5). However, it is still unknown how much of this connectivity would be due to changes in ENSO character on its own as some authors claim (Jiang et al. 2021) and how much would be related to changes in other interannual modes in other tropical basins. Due to the temporal limitation of available observations, historical and pi-control simulations with the CMIP6 initiative can provide a climate benchmark scenario to further investigate this issue. This could be the subject of further study by the authors. In addition, changes in ENSO mechanisms in different periods could also be caused by changes in the Walker circulation, which could be related to our results (Thual and Dewitte 2023). The processes behind the ENSO development during different periods and the connection with the other basins using observations must be studied in depth using model experiments, being out of the scope of this work and the aim of future work.

The findings of this study underscore the potential practical applications of the study's results in enhancing our understanding and predictive capabilities across various time scales. It holds significant scientific implications for identifying optimal time frames that provide valuable insights into seasonal to decadal climate predictions.

Acknowledgments. VM-G has been supported by ReSPonSe Junior Leader la Caixa Fellowship LCF/BQ/PR21/11840016, and MM-R has been supported by the Spanish program Juan de la Cierva Incorporación (IJC2019-041150-I/AEI/10.13039/501100011033) and Ramón y Cajal (RYC2022-038454-I, funded by MCIN/AEI/10.13039/501100011033 and cofunded by the FSE+, European Union). This research has been funded by the Spanish DISTROPIA (PID2021-125806NB-I00) and OFF (TED2021-130106B-I00) projects, the Multidecadal Modulations of Tropical Basin Interactions (TBI-MULMOD) project (LINKA20411), and the EU-H2020 TRIATLAS project (Grant Agreement 817578). The authors also thank ECMWF for providing ERA-20C reanalysis data and the NOAA Extended Reconstructed SST V5 data provided by the NOAA PSL, Boulder, Colorado, and the Met Office Hadley Centre for the SST observational datasets.

Data availability statement. SST from ERSST.v5 is available at https://psl.noaa.gov/data/gridded/data.noaa.ersst.v5.html. SST from HadISSTv1.1 is available at https://www.metoffice.gov.uk/hadobs/hadisst/data/download.html. ERA-20C reanalysis data are available at https://www.ecmwf.int/en/forecasts/dataset/ecmwf-reanalysis-20th-century. Ocean reanalysis SODA data are available at http://www.soda.umd.edu/.

REFERENCES

An, S.-I., and B. Wang, 2000: Interdecadal change of the structure of the ENSO mode and its impact on the ENSO frequency. *J. Climate*, **13**, 2044–2055, https://doi.org/10.1175/1520-0442(2000)013<2044:ICOTSO>2.0.CO;2.

Annamalai, H., S. Kida, and J. Hafner, 2010: Potential impact of the tropical Indian Ocean–Indonesian seas on El Niño characteristics. *J. Climate*, **23**, 3933–3952, https://doi.org/10.1175/2010JCLI3396.1.

Berrisford, P., and Coauthors, 2011: The ERA-Interim Archive: Version 2.0. ERA Rep. Series 1, 23 pp., https://www.ecmwf.int/sites/default/files/elibrary/2011/8174-era-interim-archive-version-20.pdf.

Cai, W., and Coauthors, 2019: Pantropical climate interactions. *Science*, **363**, eaav4236, https://doi.org/10.1126/science.aav4236.

Carton, J. A., and B. S. Giese, 2008: A reanalysis of ocean climate using Simple Ocean Data Assimilation (SODA). *Mon. Wea. Rev.*, **136**, 2999–3017, https://doi.org/10.1175/2007MWR1978.1.

Chang, P., Y. Fang, R. Saravanan, L. Ji, and H. Seidel, 2006: The cause of the fragile relationship between the Pacific El Niño and the Atlantic Niño. *Nature*, **443**, 324–328, https://doi.org/10.1038/nature05053.

Chen, S., W. Chen, B. Yu, and Z. Li, 2022: Impact of internal climate variability on the relationship between spring northern tropical Atlantic SST anomalies and succedent winter ENSO: The role of the North Pacific Oscillation. *J. Climate*, **35**, 537–559, https://doi.org/10.1175/JCLI-D-21-0505.1.

Chen, W., R. Lu, and H. Ding, 2022: A decadal intensification in the modulation of spring western tropical Atlantic sea surface temperature to the following winter ENSO after the mid-1980s. *Climate Dyn.*, **59**, 3643–3655, https://doi.org/10.1007/s00382-022-06288-z.

Chiang, J. C. H., and A. H. Sobel, 2002: Tropical tropospheric temperature variations caused by ENSO and their influence on the remote tropical climate. *J. Climate*, **15**, 2616–2631, https://doi.org/10.1175/1520-0442(2002)015<2616:TTTVCB>2.0.CO;2.

Crespo, L. R., M. B. Rodríguez-Fonseca, I. Polo, N. Keenlyside, and D. Dommenget, 2022: Multidecadal variability of ENSO in a recharge oscillator framework. *Environ. Res. Lett.*, **17**, 074008, https://doi.org/10.1088/1748-9326/ac72a3.

Crespo-Miguel, R., I. Polo, C. R. Mechoso, B. Rodriguez-Fonseca, and F. J. Cao-García, 2023: ENSO coupling to the equatorial Atlantic: Analysis with an extended improved recharge oscillator model. *Front. Mar. Sci.*, **9**, 1001743, https://doi.org/10.3389/fmars.2022.1001743.

Dayan, H., J. Vialard, T. Izumo, and M. Lengaigne, 2014: Does sea surface temperature outside the tropical Pacific contribute to enhanced ENSO predictability? *Climate Dyn.*, **43**, 1311–1325, https://doi.org/10.1007/s00382-013-1946-y.

Ding, R., and Coauthors, 2023: North Atlantic oscillation controls multidecadal changes in the North tropical Atlantic–Pacific connection. *Nat. Commun.*, **14**, 862, https://doi.org/10.1038/s41467-023-36564-3.

Drinkwater, K. F., 2006: The regime shift of the 1920s and 1930s in the North Atlantic. *Prog. Oceanogr.*, **68**, 134–151, https://doi.org/10.1016/j.pocean.2006.02.011.

Ebisuzaki, W., 1997: A method to estimate the statistical significance of a correlation when the data are serially correlated. *J. Climate*, **10**, 2147–2153, https://doi.org/10.1175/1520-0442(1997)010<2147:AMTETS>2.0.CO;2.

Enfield, D. B., and D. A. Mayer, 1997: Tropical Atlantic sea surface temperature variability and its relation to El Niño-Southern Oscillation. *J. Geophys. Res.*, **102**, 929–945, https://doi.org/10.1029/96JC03296.

Exarchou, E., P. Ortega, B. Rodríguez-Fonseca, T. Losada, I. Polo, and C. Prodhomme, 2021: Impact of equatorial Atlantic variability on ENSO predictive skill. *Nat. Commun.*, **12**, 1612, https://doi.org/10.1038/s41467-021-21857-2.

Frauen, C., and D. Dommenget, 2012: Influences of the tropical Indian and Atlantic Oceans on the predictability of ENSO. *Geophys. Res. Lett.*, **39**, L02706, https://doi.org/10.1029/2011GL050520.

Gan, R., Q. Liu, G. Huang, K. Hu, and X. Li, 2023: Greenhouse warming and internal variability increase extreme and central Pacific El Niño frequency since 1980. *Nat. Commun.*, **14**, 394, https://doi.org/10.1038/s41467-023-36053-7.

García-Serrano, J., C. Cassou, H. Douville, A. Giannini, and F. J. Doblas-Reyes, 2017: Revisiting the ENSO teleconnection to the tropical North Atlantic. *J. Climate*, **30**, 6945–6957, https://doi.org/10.1175/JCLI-D-16-0641.1.

Giannini, A., J. C. H. Chiang, M. A. Cane, Y. Kushnir, and R. Seager, 2001: The ENSO teleconnection to the tropical Atlantic Ocean: Contributions of the remote and local SSTs to rainfall variability in the tropical Americas. *J. Climate*, **14**, 4530–4544, https://doi.org/10.1175/1520-0442(2001)014<4530:TETTTT>2.0.CO;2.

Green, B., J. Marshall, and J.-M. Campin, 2019: The 'sticky' ITCZ: Ocean-moderated ITCZ shifts. *Climate Dyn.*, **53** (1–2), 1–19, https://doi.org/10.1007/s00382-019-04623-5.

Grothe, P. R., and Coauthors, 2020: Enhanced El Niño-Southern Oscillation variability in recent decades. *Geophys. Res. Lett.*, **47**, e2019GL083906, https://doi.org/10.1029/2019GL083906.

Ham, Y.-G., J.-S. Kug, J.-Y. Park, and F.-F. Jin, 2013a: Sea surface temperature in the north tropical Atlantic as a trigger for El Niño/Southern Oscillations events. *Nat. Geos. Lett.*, **6**, 112–116, https://doi.org/10.1038/ngeo1686.

——, ——, and ——, 2013b: Two distinct roles of Atlantic SST in ENSO variability: North tropical Atlantic SST and Atlantic Niño. *Geophys. Res. Lett.*, **40**, 4012–4017, https://doi.org/10.1002/grl.50729.

Hare, S. R., and N. J. Mantua, 2000: Empirical evidence for North Pacific regime shifts in 1977 and 1989. *Prog. Oceanogr.*, **47**, 103–145, https://doi.org/10.1016/S0079-6611(00)00033-1.

Huang, B., and Coauthors, 2017: Extended Reconstructed Sea Surface Temperature version 5 (ERSSTv5): Upgrades, validations, and intercomparisons. *J. Climate*, **30**, 8179–8205, https://doi.org/10.1175/JCLI-D-16-0836.1.

Izumo, T., and Coauthors, 2010: Influence of the state of the Indian Ocean dipole on the following year's El Niño. *Nat. Geosci.*, **3**, 168–172, https://doi.org/10.1038/ngeo760.

——, M. Lengaigne, J. Vialard, J.-J. Luo, T. Yamagata, and G. Madec, 2014: Influence of Indian Ocean dipole and Pacific recharge on following year's El Niño: Interdecadal robustness. *Climate Dyn.*, **42**, 291–310, https://doi.org/10.1007/s00382-012-1628-1.

Jiang, F., W. Zhang, F.-F. Jin, M. F. Stuecker, and R. Allan, 2021: El Niño pacing orchestrates inter-basin Pacific-Indian Ocean interannual connections. *Geophys. Res. Lett.*, **48**, e2021GL095242, https://doi.org/10.1029/2021GL095242.

——, ——, ——, ——, A. Timmermann, M. J. McPhaden, J. Boucharel, and A. T. Wittenberg, 2023: Resolving the tropical Pacific/Atlantic interaction conundrum. *Geophys. Res. Lett.*, **50**, e2023GL103777, https://doi.org/10.1029/2023GL103777.

Jiang, L., and T. Li, 2021: Impacts of tropical North Atlantic and equatorial Atlantic SST anomalies on ENSO. *J. Climate*, **34**, 5635–5655, https://doi.org/10.1175/JCLI-D-20-0835.1.

——, ——, and Y.-G. Ham, 2022: Critical role of tropical North Atlantic SSTA in boreal summer in affecting subsequent ENSO evolution. *Geophys. Res. Lett.*, **49**, e2021GL097606, https://doi.org/10.1029/2021GL097606.

——, ——, and ——, 2023: Asymmetric impacts of El Niño and La Niña on equatorial Atlantic warming. *J. Climate*, **36**, 193–212, https://doi.org/10.1175/JCLI-D-22-0158.1.

Keenlyside, N. S., H. Ding, and M. Latif, 2013: Potential of equatorial Atlantic variability to enhance El Niño prediction. *Geophys. Res. Lett.*, **40**, 2278–2283, https://doi.org/10.1002/grl.50362.

Klein, S. A., B. J. Soden, and N.-C. Lau, 1999: Remote sea surface temperature variations during ENSO: Evidence for a tropical atmospheric bridge. *J. Climate*, **12**, 917–932, https://doi.org/10.1175/1520-0442(1999)012<0917:RSSTVD>2.0.CO;2.

Krishnamurthy, V., and B. P. Kirtman, 2003: Variability of the Indian Ocean: Relation to monsoon and ENSO. *Quart. J. Roy. Meteor. Soc.*, **129**, 1623–1646, https://doi.org/10.1256/qj.01.166.

Latif, M., and A. Grötzner, 2000: The equatorial Atlantic oscillation and its response to ENSO. *Climate Dyn.*, **16**, 213–218, https://doi.org/10.1007/s003820050014.

Lau, N.-C., and M. J. Nath, 2003: Atmosphere–ocean variations in the Indo-Pacific sector during ENSO episodes. *J. Climate*, **16**, 3–20, https://doi.org/10.1175/1520-0442(2003)016<0003:AOVITI>2.0.CO;2.

Li, J., C. Sun, and F.-F. Jin, 2013: NAO implicated as a predictor of Northern Hemisphere mean temperature multidecadal variability. *Geophys. Res. Lett.*, **40**, 5497–5502, https://doi.org/10.1002/2013GL057877.

Losada, T., and B. Rodríguez-Fonseca, 2016: Tropical atmospheric response to decadal changes in the Atlantic Equatorial Mode. *Climate Dyn.*, **47**, 1211–1224, https://doi.org/10.1007/s00382-015-2897-2.

——, ——, C. R. Mechoso, E. Mohino, and A. Castaño-Tierno, 2022: Changes in interannual tropical Atlantic–Pacific basin interactions modulated by a South Atlantic cooling. *J. Climate*, **35**, 4403–4416, https://doi.org/10.1175/JCLI-D-21-0546.1.

Lübbecke, J. F., and M. J. McPhaden, 2012: On the inconsistent relationship between Pacific and Atlantic Niños. *J. Climate*, **25**, 4294–4303, https://doi.org/10.1175/JCLI-D-11-00553.1.

Luo, J.-J., R. Zhang, S. K. Behera, Y. Masumoto, F.-F. Jin, R. Lukas, and T. Yamagata, 2010: Interaction between El Niño and extreme Indian Ocean dipole. *J. Climate*, **23**, 726–742, https://doi.org/10.1175/2009JCLI3104.1.

Ma, J., H. Xu, J.-J. Luo, and S. Chen, 2022: Impact of tropical Atlantic SST anomaly on ENSO in the NUIST-CFS1.0 hindcasts. *Int. J. Climatol.*, **42**, 6055–6071, https://doi.org/10.1002/joc.7577.

Martín-Gómez, V., and M. Barreiro, 2015: Analysis of oceans' influence on spring time rainfall variability over Southeastern South America during the 20th century. *Int. J. Climatol.*, **36**, 1344–1358, https://doi.org/10.1002/joc.4428.

Martín-Rey, M., B. Rodríguez-Fonseca, I. Polo, and F. Kucharski, 2014: On the Atlantic–Pacific Niños connection: A multidecadal modulated mode. *Climate Dyn.*, **43**, 3163–3178, https://doi.org/10.1007/s00382-014-2305-3.

Martín-Rey, M., B. Rodríguez-Fonseca, and I. Polo, 2015: Atlantic opportunities for ENSO prediction. *Geophys. Res. Lett.*, **42**, 6802–6810, https://doi.org/10.1002/2015GL065062.

Martín-Rey, M., I. Polo, B. Rodríguez-Fonseca, T. Losada, and A. Lazar, 2018: Is there evidence of changes in tropical Atlantic variability modes under AMO phases in the observational record? *J. Climate*, **31**, 515–536, https://doi.org/10.1175/JCLI-D-16-0459.1.

McPhaden, M. J., S. E. Zebiak, and M. H. Glantz, 2006: ENSO as an integrating concept in earth science. *Science*, **314**, 1740–1745, https://doi.org/10.1126/science.1132588.

Miller, A. J., D. R. Cayan, T. P. Barnett, N. E. Graham, and J. M. Oberhuber, 1994: The 1976-77 climate shift of the Pacific Ocean. *Oceanography*, **7** (1), 21–26, https://doi.org/10.5670/oceanog.1994.11.

Park, J.-H., J.-S. Kug, Y.-M. Yang, M.-K. Sung, S. Kim, H.-J. Kim, H.-J. Park, and S.-I. An, 2023a: Distinct decadal modulation of Atlantic-Niño influence on ENSO. *npj Climate Atmos. Sci.*, **6**, 105, https://doi.org/10.1038/s41612-023-00429-9.

——, S.-W. Yeh, J.-S. Kug, Y.-M. Yang, H.-S. Jo, H.-J. Kim, and S.-I. An, 2023b: Two regimes of inter-basin interactions between the Atlantic and Pacific Oceans on interannual timescales. *npj Climate Atmos. Sci.*, **6**, 13, https://doi.org/10.1038/s41612-023-00332-3.

Poli, P., and Coauthors, 2016: ERA-20C: An atmospheric reanalysis of the twentieth century. *J. Climate*, **29**, 4083–4097, https://doi.org/10.1175/JCLI-D-15-0556.1.

Polo, I., M. Martín-Rey, B. Rodríguez-Fonseca, F. Kucharski, and C. R. Mechoso, 2015: Processes in the Pacific La Niña onset triggered by the Atlantic Niño. *Climate Dyn.*, **44**, 115–131, https://doi.org/10.1007/s00382-014-2354-7.

Rayner, N. A., D. E. Parker, E. B. Horton, C. K. Folland, L. V. Alexander, D. P. Rowell, E. C. Kent, and A. Kaplan, 2003: Global analyses of sea surface temperature, sea ice, and night marine air temperature since the late nineteenth century. *J. Geophys. Res.*, **108**, 4407, https://doi.org/10.1029/2002JD002670.

Rodríguez-Fonseca, B., I. Polo, J. García-Serrrano, T. Losada, E. Mohino, C. R. Mechoso, and F. Kucharski, 2009: Are Atlantic Niños enhancing Pacific ENSO events in recent decades? *Geophys. Res. Lett.*, **36**, L20705, https://doi.org/10.1029/2009GL040048.

——, Y.-G. Ham, S.-K. Lee, M. Martín-Rey, I. P. Sánchez, and R. R. Rodrigues, 2020: Interacting interannual variability of the Pacific and Atlantic Oceans. *Interacting Climates of Ocean Basins: Observations, Mechanisms, Predictability, and Impacts*, C. Mechoso, Ed., Cambridge University Press, 120–152, https://doi.org/10.1017/9781108610995.005.

Rong, X., R. Zhang, and T. Li, 2010: Impacts of Atlantic sea surface temperature anomalies on Indo-East Asian summer monsoon-ENSO relationship. *Chin. Sci. Bull.*, **55**, 2458–2468, https://doi.org/10.1007/s11434-010-3098-3.

Saji, N. H., B. N. Goswami, P. N. Vinayachandran, and T. Yamagata, 1999: A dipole mode in the tropical Indian Ocean. *Nature*, **401**, 360–363, https://doi.org/10.1038/43854.

Thual, S., and B. Dewitte, 2023: ENSO complexity controlled by zonal shifts in the Walker circulation. *Nat. Geosci.*, **16**, 328–332, https://doi.org/10.1038/s41561-023-01154-x.

Timmermann, A., and Coauthors, 2018: El Niño–Southern Oscillation complexity. *Nature*, **559**, 535–545, https://doi.org/10.1038/s41586-018-0252-6.

Trascasa-Castro, P., Y. Ruprich-Robert, F. Castruccio, and A. C. Maycock, 2021: Warm phase of AMV damps ENSO through weakened thermocline feedback. *Geophys. Res. Lett.*, **48**, e2021GL096149, https://doi.org/10.1029/2021GL096149.

Tsonis, A. A., K. Swanson, and S. Kravtsov, 2007: A new dynamical mechanism for major climate shifts. *Geophys. Res. Lett.*, **34**, L13705, https://doi.org/10.1029/2007GL030288.

Wade, M., B. Rodríguez-Fonseca, M. Martín-Rey, A. Lazar, J. López-Parages, and A. T. Gaye, 2022: Interdecadal changes in SST variability drivers in the Senegalese-upwelling: The impact of ENSO. *Climate Dyn.*, **60**, 667–685, https://doi.org/10.1007/s00382-022-06311-3.

Wang, J.-Z., and C. Wang, 2021: Joint boost to super El Niño from the Indian and Atlantic Oceans. *J. Climate*, **34**, 4937–4954, https://doi.org/10.1175/JCLI-D-20-0710.1.

Wang, L., J.-Y. Yu, and H. Paek, 2017: Enhanced biennial variability in the Pacific due to Atlantic capacitor effect. *Nature*, **8**, 14887, https://doi.org/10.1038/ncomms14887.

Wang, X., and C. Wang, 2014: Different impacts of various El Niño events on the Indian Ocean dipole. *Climate Dyn.*, **42**, 991–1005, https://doi.org/10.1007/s00382-013-1711-2.

Webster, P. J., A. M. Moore, J. P. Loschnigg, and R. R. Leben, 1999: Coupled ocean–atmosphere dynamics in the Indian Ocean during 1997–98. *Nature*, **401**, 356–360, https://doi.org/10.1038/43848.

Weisheimer, A., M. A. Balmaseda, T. N. Stockdale, M. Mayer, S. Sharmila, H. Hendon, and O. Alves, 2022: Variability of ENSO forecast skill in 2-year global reforecasts over the 20th century. *Geophys. Res. Lett.*, **49**, e2022GL097885, https://doi.org/10.1029/2022GL097885.

Wu, R., M. Lin, and H. Sun, 2020: Impacts of different types of El Niño and La Niña on northern tropical Atlantic sea surface temperature. *Climate Dyn.*, **54**, 4147–4167, https://doi.org/10.1007/s00382-020-05220-7.

Yu, J., T. Li, Z. Tan, and Z. Zhu, 2016: Effects of tropical North Atlantic SST on tropical cyclone genesis in the western North Pacific. *Climate Dyn.*, **46**, 865–877, https://doi.org/10.1007/s00382-015-2618-x.

Zhang, W., F. Jiang, M. F. Stuecker, F.-F. Jin, and A. Timmermann, 2021: Spurious north tropical Atlantic precursors to El Niño. *Nat. Commun.*, **12**, 3096, https://doi.org/10.1038/s41467-021-23411-6.